Energy & Environmental Science

ROYAL SOCIETY
OF **CHEMISTRY**

PAPER
Marco Siniscalchi, Chris R. M. Grovenor *et al.*
Initiation of dendritic failure of LLZTO *via* sub-surface
lithium deposition

ROYAL SOCIETY
OF CHEMISTRY

PAPER

Check for updates

Initiation of dendritic failure of LLZTO *via* sub-surface lithium deposition†

Marco Siniscalchi, [ID] *[ab] Yifu Shi,[a] Guanchen Li,[c] Joshua S. Gibson, [ID] [abd] Robert S. Weatherup, [ID] [ab] Ruy S. Bonilla, [ID] [a] Susannah C. Speller[a] and Chris R. M. Grovenor*[ab]

The occurrence of lithium deposition in occluded spaces within ceramic electrolytes due to electronic leakage currents can jeopardise the commercialization of power-dense solid-state batteries. Here, we utilize plasma-FIB serial sectioning to visualize the surface and sub-surface of a garnet solid electrolyte (LLZTO) after lithium plating. We study the morphology of surface spallation cracks, which represent the initial stage of dendrite formation. Employing a LiMg anode, we track the magnesium diffusion around these surface cracks with EDS. The absence of magnesium in early-stage cracks suggests they form due to the pressure build-up from the deposition of pure lithium in occluded pores near the electrolyte surface. These spallation cracks act as current focusing and stress concentration hot spots. Electron beam induced current imaging demonstrates that short-circuiting lithium dendrites grow from the spallations during plating. Thus, the sub-surface deposition of lithium is a possible explanation for the initiation of lithium dendrites in LLZTO.

Broader context

Solid-state batteries featuring a lithium metal anode hold promise for enhancing battery energy density, power density and safety compared to traditional lithium-ion batteries. However, a critical obstacle hindering the commercialization of solid-state batteries lies in the growth of lithium dendrites through the solid electrolyte during charging, resulting in short circuits. Recently, there has been significant attention on the mechanism triggering dendrite initiation. Some reports suggest that lithium metal can plate inside the solid electrolyte due to electric current leakage in occluded pores or along grain boundaries, but direct experimental evidence is lacking. Here, we investigate the deposition of lithium in the solid electrolyte sub-surface using plasma-FIB tomography. Magnesium is used as the tracer element in the plating electrode to confirm that pure lithium metal can plate in isolated sub-surface pores, resulting in pressure buildup and ultimately initiating the dendritic process. This work provides the most direct visualization of internal lithium plating, shedding light on the mechanism behind dendrite formation.

Lithium metal solid-state batteries have the potential to offer improved energy and power densities, as well as enhanced safety, compared to conventional lithium-ion batteries.[1,2] However, the formation of lithium filaments or 'dendrites', which can penetrate through the solid electrolyte (SE) and short circuit the cell at small nominal current densities, remains a major obstacle to the widespread use of solid-state batteries.[3,4] The mechanism of lithium dendrite formation in SEs is still

subject to debate, but it is generally agreed that they tend to nucleate preferentially at current hot spots located at the interface between the plating lithium metal electrode and the SE.[5,6] Such hot spots can arise due to inhomogeneities, such as grain boundaries, microcracks on the SE surface, or regions of poor interfacial solid–solid contact.[7–9] In these spots, the pressure build-up from the plated lithium can lead to the formation of a crack or to the extension of a pre-existing microcrack, creating a self-sustaining mechanism that cascades through the SE.[10,11] Recently it has been suggested that lithium can also plate internally in occluded regions within the SE, without direct electrical connection to the plating electrode.[12–16] While the electrical conductivity of bulk SEs is too low to allow isolated lithium plating, with values between 10^{-8} and 10^{-10} S cm^{-1},[17–19] reduced band gaps at grain boundaries and pore surfaces could allow current leakage and make these regions susceptible to this

[a] *Department of Materials, University of Oxford, Oxford, OX1 3PH, UK*

[b] *The Faraday Institution, Didcot, OX11 0RA, UK.*
E-mail: marco.siniscalchi@materials.ox.ac.uk, chris.grovenor@materials.ox.ac.uk

[c] *James Watt School of Engineering, University of Glasgow, Glasgow, G12 8QQ, UK*

[d] *Oxford Centre for Energy Materials Research, Henry Royce Institute, Oxford, OX1 3PH, UK*

This journal is © The Royal Society of Chemistry 2024

Energy Environ. Sci., 2024, **17**, 2431–2440 | **2431**

phenomenon.[20–25] The pressure build-up resulting from this isolated lithium deposition could lead to local mechanical damage of the SE, promoting the propagation of lithium dendrites. However, there is a lack of literature data that clearly demonstrate the feasibility of isolated lithium deposition. In general, distinguishing isolated lithium deposits from lithium dendrites connected to the plating electrode is challenging. X-ray tomography has been the primary tool employed to obtain three-dimensional views of the SE and to investigate internal lithium deposition, but it has limitations, including low resolution and low phase contrast between metallic lithium and ceramic materials.[26–28] Further evidence is therefore required to confirm that isolated lithium deposition is possible in different SE materials, and to demonstrate the relative importance of the two degradation modes, namely dendrite propagation through electrical degradation or classic mechanical fracture.

We here employed high-resolution plasma focused ion beam (FIB) to examine the surface and sub-surface regions of $Li_{6.4}La_3Zr_{1.4}Ta_{0.6}O_{12}$ (LLZTO) SE pellets after lithium plating.

Circular pothole cracks or 'spallations' can be found on the LLZTO surface after peeling off the plating electrode. Plasma-FIB sectioning shows that these spallations are filled with freshly plated lithium metal, which appears to have cracked the SE surface from within. To confirm that the freshly plated lithium can be physically isolated from the plating electrode, we used a plating electrode containing 10 at% of Mg and tracked magnesium diffusion through the plated lithium by EDS analysis. While magnesium can diffuse in the plated lithium connected to the LiMg electrode, pure lithium metal is found filling the early-stage cracks in the sub-surface volume. In addition, to gain a better understanding of the relationship between the isolated lithium deposition and the propagation of lithium dendrites, we employed electron beam induced current imaging (EBIC) on LLZTO pellets that were short-circuited by lithium dendrites. This technique uses the SEM electron beam to probe the electrical continuity between the surface cracks on the plating side and the lithium counter electrode. With this technique we confirmed that the spallation cracks on the
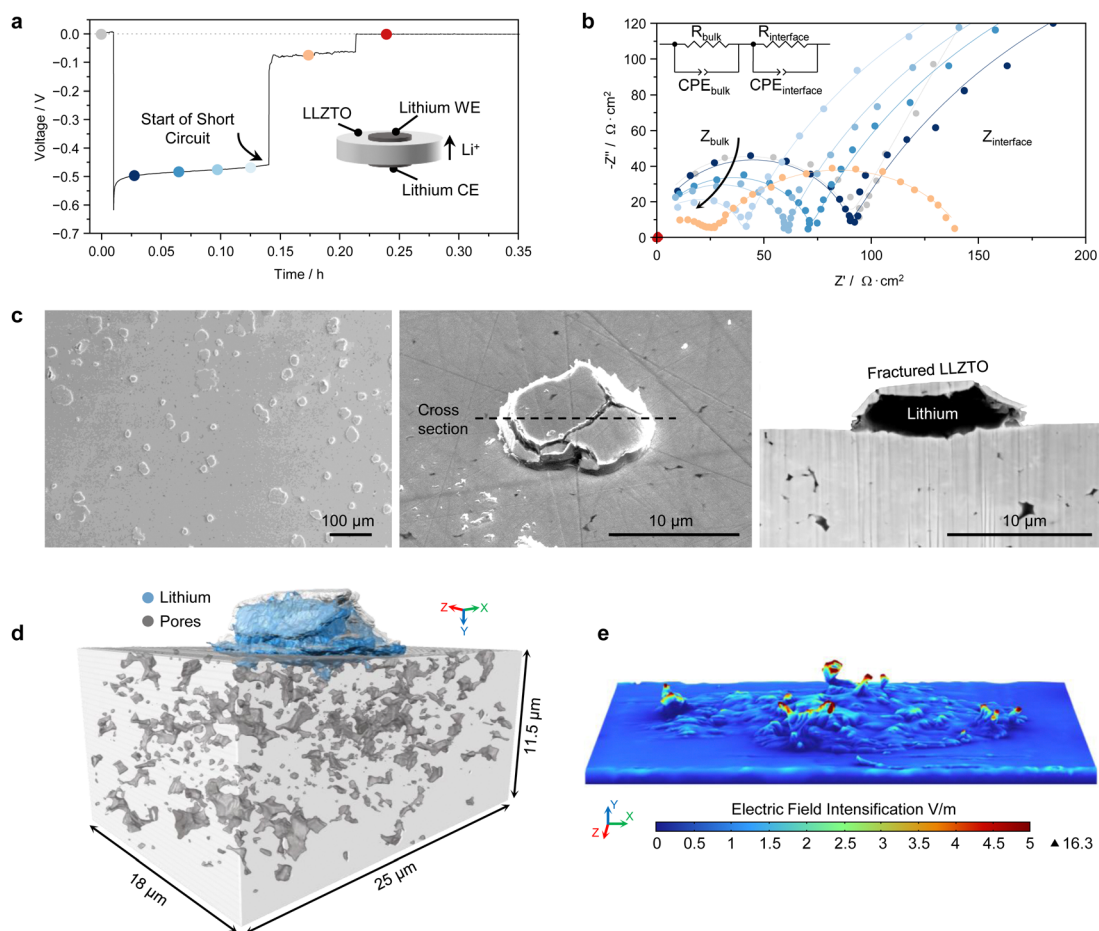

Fig. 1 Spallation cracks on the LLZTO surface after lithium plating. (a) Voltage *versus* time plot for the plating step of a Li/LLZTO/Li cell at 0.5 mA cm^{-2} and 5 MPa stack pressure. The inset shows the symmetric cell setup. (b) GEIS spectra corresponding to each coloured dot in (a) and the equivalent circuit model used to fit them. (c) Secondary electron images of the LLZTO surface after short-circuit and peeling off the Li-WE, with a cross-section showing the fractured LLZTO surface and the lithium metal below it. (d) Three-dimensional view of the spallation crack shown in (c) and of the sub-surface porosity. (e) Finite element modeling of the electric field distribution based on the reconstructed spallation crack in (d) (note the inversion of the direction of the *y* axis).

LLZTO surface can be the origin of short-circuiting lithium dendrites. Therefore, we propose that the isolated lithium deposition in the sub-surface region of the LLZTO pellet causes the surface cracking and that the plating current focusing at these locations facilitates the propagation of lithium dendrites from the crack tip into the SE.

Spalling of LLZTO during lithium plating

LLZTO is one of the most promising and widely studied SE candidates thanks to its relatively high room temperature ionic conductivity of ~ 1 mS cm^{-1}, low electronic conductivity of 10^{-8} S cm^{-1}, and excellent electrochemical stability with lithium metal.[29] See Fig. S1 and S2 (ESI†) for a full characterisation of the LLZTO pellets used in this study.

However when a Li/LLZTO/Li symmetric cell is cycled at a current density exceeding a 'critical' value, lithium dendrites can grow from the electroplating electrode (Li-WE in our setup in Fig. 1a) and reach the stripping electrode (Li-CE), effectively creating a short-circuit. This causes all the current to flow through the short-circuit, resulting in cell failure. The growth of the lithium dendrite can be detected during *operando* galvanostatic electrochemical impedance spectroscopy (GEIS) during a single plating step as shown in Fig. 1b.[30] A typical GEIS spectrum of a Li/LLZTO/Li cell contains two semicircles, one at high-frequency and one at low-frequency, which can be assigned to the bulk LLZTO and to the Li/LLZTO interface respectively.[5] During cycling, the bulk LLZTO contribution gradually decreases in magnitude (see also Fig. S3, ESI†), indicating a reduction of the Ohmic resistance, and therefore of the effective distance, between the electrodes. This is due to lithium deposition in the SE, in the form of either lithium dendrites or isolated lithium deposits. Eventually, a sudden impedance drop demonstrates the complete short-circuit of the cell.

The Li/LLZTO/Li cell was assembled without any pre-treatment that improves the Li/LLZTO interfacial contact, such as removing the Li_2CO_3 and LiOH contamination that promptly forms on the LLZTO surface when in contact with trace H_2O and CO_2 in the glovebox.[31] XPS of a LLZTO pellet before cell assembly is reported in Fig. S4 (ESI†). The surface contaminants are lithio-phobic and cause incomplete contact between lithium and LLZTO, resulting in a R_{int} before cycling of about 2000 Ω cm^{-2} (grey data points in Fig. 1b and in Fig. S3, ESI†). Soon after the onset of plating, R_{int} decreases to about 500 Ω cm^{-2} because the plated lithium improves the contact at the Li-WE side. Afterwards, R_{int} remains almost constant while the bulk resistance decreases, until the start of the short circuit. We intentionally used a lithio-phobic LLZTO so that we could more easily remove the Li-WE after the cell short-circuit and inspect the LLZTO surface. However, a similarly large R_{int} can also develop during stripping of a Li/LLZTO interface with a near-zero starting R_{int}, which we obtained by chemically removing the contaminants on the LLZTO surface (Fig. S4 and S5, ESI†).[32] In this case the large R_{int} develops due to voiding at the

Li/LLZTO interface, so that the short circuit occurs on the subsequent plating step.[33] As shown later, a larger nominal current density may be required to drive lithium dendrites through a cell with a smaller R_{int}, but none of our cells seems to avoid short-circuiting failure under commercially relevant cycling conditions.

After peeling off the Li-WE, circular cracks ranging from ~ 5 to 100 μm in diameter can be observed on the LLZTO surface (Fig. 1c and Fig. S6, ESI†). Similar cracks have been recently reported in different SEs as spallations or spallation cracks.[34–38] The sectioning of one of these surface spallation cracks shows that it contains freshly plated lithium metal, which seems to have extruded from beneath the surface and out of the crack. Similar cracks are also observed when the Li-WE is left on and the buried Li/LLZTO interface is cross-sectioned with plasma-FIB (Fig. S7, ESI†), therefore we believe that any mechanical damage introduced by peeling the Li-WE off is not the cause of these features. Clear indentations can be observed on the surface of the peeled Li-WE where the fractured LLZTO surface was pushed into the soft lithium (Fig. S6d, ESI†). Furthermore, the absence of cracks in the LLZTO pellet after cell assembly (Fig. S8, ESI†) indicates they develop during cycling.

Plasma-FIB serial sectioning allows us to study the three-dimensional view of such cracks, as in Fig. 1d. A complete account on the three-dimensional reconstruction procedure is reported in Note S1 (ESI†). The cracks seem to be mainly intergranular, running through formerly isolated sub-surface pores located at grain boundary triple junctions (see Movie S1, ESI†). These pores, which typically have a concave geometry with pointed edges, can contain lithium metal and therefore represent a sharp lithium protrusion into the SE where the current would be geometrically concentrated. Finite element modeling of the electric field was carried out based on the crack surface reconstructed in Fig. 1d (see Methods section), demonstrating that the electric field at the tip of the spallation crack can be much greater than the electric field in the bulk of the SE (Fig. 1e). The electric field is directly proportional to the local current density, so the plating current density in that region must have been larger than the nominally applied value. The volume of lithium plated in the spallation crack in Fig. 1c and d is indeed larger than that expected from the nominal plated capacity for this specific sample (notice that the cross-sectional images in the manuscript are tilted by $52°$ so the true vertical dimension is obtained by multiplying by 1.27). Considering that larger and deeper spallation cracks can be found on the LLZTO surface (Fig. S6c, ESI†), these surface cracks evidently represent current intensification hot spots as well as stress concentration points, and could be the preferential location for the growth of lithium dendrites.

Locating the short-circuiting dendrite

X-ray tomography may be used to visualize the lithium dendrites, but the X-ray attenuating properties of LLZTO make imaging of buried lithium challenging. Therefore, to investigate the presence

This journal is © The Royal Society of Chemistry 2024

Energy Environ. Sci., 2024, **17**, 2431–2440 | **2433**

of lithium dendrites originating from the surface cracks we used Electron Beam Induced Current (EBIC) imaging. EBIC is a SEM-based technique typically used to characterize semiconductor devices.[39] During EBIC imaging, a W microprobe is connected to a spallation crack on the LLZTO surface and then to the SEM sample stage through a current amplifier, while the Li-CE is in contact with the SEM sample stage (Fig. 2a). A lithium dendrite originating from the spallation crack and reaching down to the Li-CE would effectively close the electrical circuit. When the electron beam illuminates the spallation crack region, a portion of the excess electrons are collected at the device contacts, giving rise to a current. By scanning the electron beam, a two dimensional map of collected current is constructed. The EBIC image in Fig. 2c shows a spallation crack giving dark contrast as excess electrons are collected by the sample stage through the lithium dendrite, confirming that the lithium in this surface crack is electrically connected to a short-circuiting lithium dendrite proceeding from the surface crack. The *I–V* curve in Fig. 2d measured with the EBIC setup shows a lithium dendrite resistance of 440 Ω, which matches well with the resistance of the cell after short-circuiting of 487 Ω (Fig. S9, ESI†). Assuming a straight pure lithium dendrite running through the SE pellet, its diameter would be $\sim$500 nm. In reality, a network of irregular filaments with smaller diameter usually extends through the LLZTO pellet.[35] After EBIC analysis, we used plasma-FIB to cross-section the sub-surface region and identified a narrow crack (50–100 nm in diameter) beneath the surface spallation running through the LLZTO porosity (Fig. 2b and Fig. S10, ESI†). In some cases, a lithium-filled macroscopic

crack could be observed running from the surface spallation cracks through the whole SE pellet (Fig. S11, ESI†). Thus this use of EBIC imaging shows that the short-circuiting failure of the SE likely originates from the tip of the surface spallation cracks, where the current density is at its maximum.

Using magnesium to look for isolated lithium deposits

The growth of a transverse dendrite crack from a surface spallation is consistent with previous work on Li_6PS_5Cl SE.[34] However, the formation mechanism of the spallation cracks has been so far unclear. As these surface features seem to play an important role in the initiation of dendritic cell failure, we wanted to study their origin in more detail. The morphology of early-stage spallation cracks, such as those depicted in Fig. S6a (ESI†), suggests an internal and isolated origin of the pressure build-up that ultimately causes the crack to open to the LLZTO surface. LLZTO spalling behaviour is similarly observed when no external stack pressure is applied to the cell (Fig. S12, ESI†), so the pressure seems to build up in the spallation cracks independently of the external stack pressure. Moreover, since the population density of the spallation cracks decreases with increasing pellet density (Fig. S13, ESI†), we propose that this pressure build-up may occur in occluded sub-surface porosity. Therefore, we sectioned early-stage spallations to search for isolated internal lithium deposition. However, despite the high
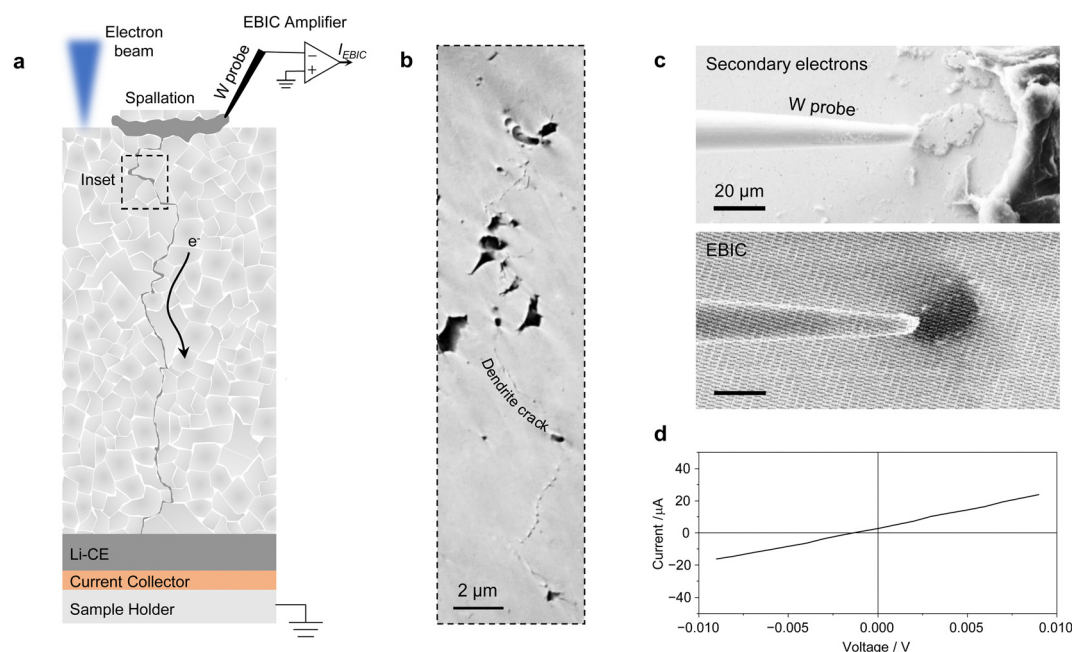

Fig. 2 EBIC imaging of a surface spallation connected to the short-circuiting dendrite. (a) Schematic of the experimental setup: a W microprobe is in contact with the lithium metal extruding from a surface spallation crack. Excess electrons from the electron beam can be collected at the Li-CE through the short-circuiting lithium dendrite, with the circuit completed through the W microprobe and the current amplifier. (b) A dendrite crack can be observed beneath the spallation crack after cross sectioning. (c) Secondary electron and EBIC images showing a current contrast arising at the surface spallation, indicating electrical connection between the spallation and the Li-CE. The scale bars are 20 μm. (d) *I–V* curve of the lithium dendrite showing resistive behaviour.

spatial resolution of plasma-FIB images, a narrow lithium path invisible to SEM could still connect the lithium in the surface crack to the Li-WE even when the deposit appears isolated. Therefore, instead of a pure Li-WE we used a LiMg-WE containing 10 at% Mg. Magnesium has a wide solubility range in lithium and their inter-diffusion is quite fast.[40] Hence, magnesium will spontaneously diffuse into plated lithium that is physically, *i.e.* electrically, connected to the LiMg-WE because of the Mg compositional gradient, where it can be unequivocally detected by EDS. Moreover, the addition of 10 at% Mg only marginally increases the anode voltage by a few meV and does not alter the electrodeposition behavior (see GEIS in Fig. S14, ESI†).[41] A LiMg/LLZTO/Li cell was assembled, and lithium was plated at the LiMg/LLZTO interface until short-circuiting occurred. The LiMg-WE was peeled off after a period of at least 15 days to leave the magnesium time to diffuse through the freshly plated lithium. Fig. 3a shows three spallation cracks that were found on the same LLZTO surface and represent different stages of crack growth. The first spallation crack has not yet fully developed. The plasma-FIB cross-sectioning reveals that the crack already contains some lithium metal, although not throughout the entire crack (Fig. 3b). No magnesium signal could be detected, suggesting that the lithium metal in the crack has not been in direct contact with the LiMg-WE. By contrast, magnesium was able to diffuse into the lithium contained in the second crack, which thus must have been in contact with the LiMg electrode. Finally, the fully developed spallation crack contains a large amount of lithium metal giving a strong magnesium EDS signal. The three-dimensional reconstructions of these spallation cracks obtained by automated serial sectioning of LLZTO are reported in Fig. 3c and Movie S2 (ESI†). We cannot rule out the possibility that the magnesium content in the early-stage spallation crack may be below the sensitivity of the EDS analysis, but magnesium seems to easily diffuse in narrow Li-filled cracks as shown in the second spallation in Fig. 3. In this case, magnesium was also detected in
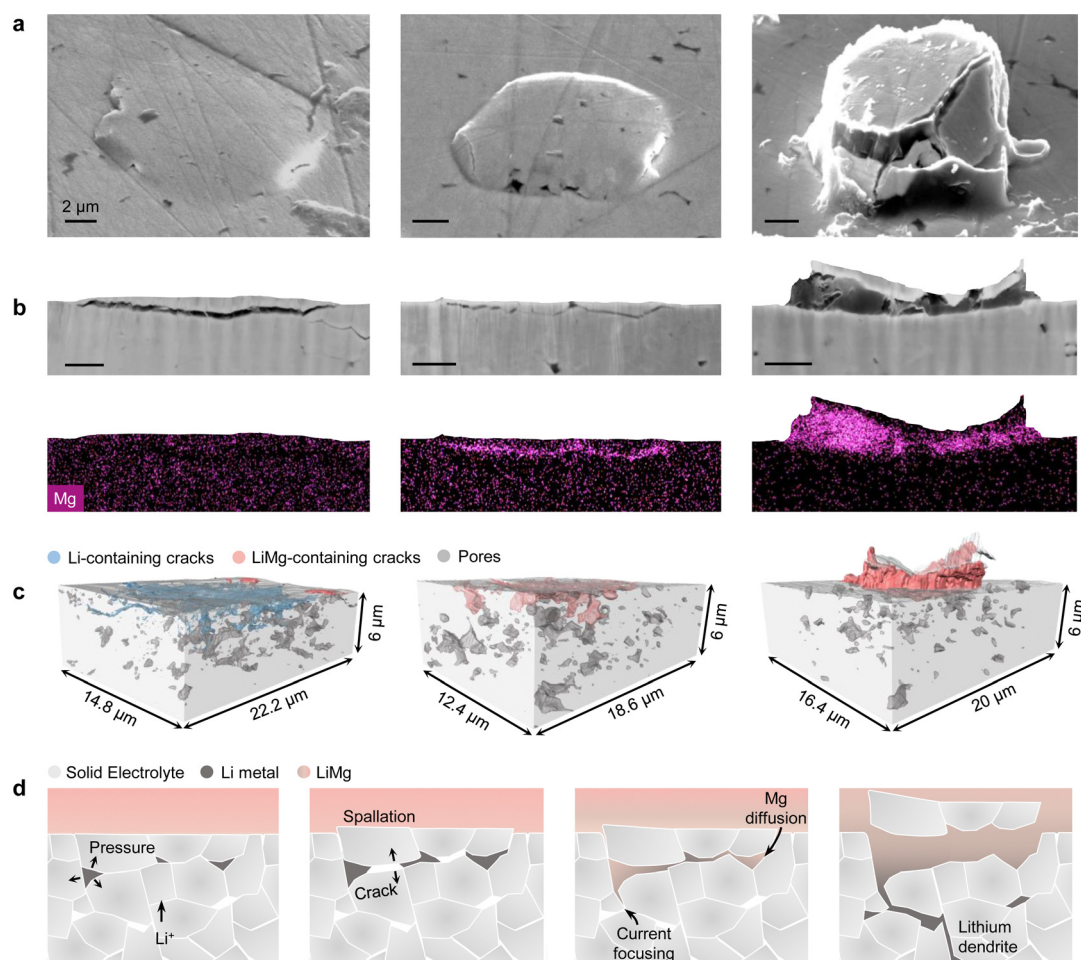

Fig. 3 Different stages of the formation of surface spallations at the LiMg/LLZTO interface. (a) Secondary electron images of three different spallation cracks found on the LLZTO surface after short-circuiting of a LiMg/LLZTO/Li cell and peeling off the LiMg-WE. (b) Cross-sectional secondary electron and EDS images showing the diffusion of magnesium in some Li-filled cracks, those in which lithium was physically connected to the LiMg-WE. The Pt-C protective layer deposited prior to plasma-FIB sectioning has slightly modified the appearance of the fractured LLZTO. (c) Three-dimensional views of the surface cracks identifying those filled with Li or LiMg. (d) Schematic with the proposed formation mechanism and evolution of a spallation crack at the LiMg/LLZTO interface.

This journal is © The Royal Society of Chemistry 2024

Energy Environ. Sci., 2024, **17**, 2431–2440 | **2435**

porosity further away from the LLZTO surface and connected to the spallation through a very thin crack (Fig. S18, ESI†). The proposed evolution of a spallation crack with a LiMg electrode is reported in the schematic in Fig. 3d. Lithium plating in the sub-surface porosity of the LLZTO pellet leads to an internal pressure build-up exceeding the fracture strength of the SE, and a crack is formed. As more lithium is plated in the crack, the fractured LLZTO surface is pushed into the soft LiMg-WE and the lithium in the crack connects to the lithium electrode creating a channel for magnesium diffusion. From this moment onward, lithium will preferentially plate inside these cracks where it is confined in a small volume, and the significant pressure build-up can drive further crack growth.

We believe our results show that LLZTO can be susceptible to isolated lithium deposition. Moreover, we suggest that the presence of spallation cracks on the SE surface can be evidence for the ability of lithium to deposit in occluded sub-surface porosity. We also found spallation cracks on the surface of Na β-Al_2O_3 (Fig. S15, ESI†). Na β-Al_2O_3 SEs were extensively studied before the advent of the lithium-ion cells and are already known to be susceptible to isolated internal deposition of sodium metal.[42,43]

Current dependency of the spalling process

The conditions for internal lithium deposition seem to be met almost instantly upon application of current to the cell, as early-stage spallation cracks have been observed at the LiMg/LLZTO interface after only 10 μA h cm^{-2} of plating (Fig. 4a). A cryo-stage was used for plasma-FIB sectioning of these

spallations, to ensure the presence of lithium is not due to beam damage.[44] Lithium metal is already present in the cracks, even though the cell has not fully short-circuited (Fig. S16, ESI†). Magnesium was not detected in these early-stage spallation cracks. Therefore as soon as the current is applied, the local current value immediately diverges from the nominal average one as the current intensifies at the crack tips.

At this point, we wanted to investigate whether there is a minimum current density for the formation of surface spallations. As the starting interfacial resistance R_{int} between the lithium electrode and the LLZTO pellets with surface Li_2CO_3 and LiOH contaminants was quite large (see Fig. 1b), the local plating current density was unknown. Therefore, we chemically removed the surface contaminants to obtain a near-zero starting R_{int} between lithium and LLZTO (Fig. S17, ESI†), so that the local plating current density should not diverge too much from the nominally applied value. We plated 1 mA h cm^{-2} of capacity at different current densities and subsequently dissolved the Li-WE in ethanol to reveal the LLZTO surface. While surface spallations and dendrites readily formed with an untreated lithio-phobic LLZTO pellet at a nominally applied current density of 0.5 mA cm^{-2}, no spallations are now visible on the lithio-philic LLZTO pellet cycled at 0.5 and 2.5 mA cm^{-2} and the voltage is stable (Fig. 4b). Instead, a few spallation craters are visible on the surface of lithio-philic LLZTO after plating at 5 mA cm^{-2} (Fig. 4c). The craters are close to the edge of the Li-WE, where the current density is largest. Notice that no full short-circuit occurred at 5 mA cm^{-2} and 1 mA h cm^{-2} of plated capacity, even though the voltage instability indicates some level of dendritic growth. This also shows that decreasing the starting R_{int} is an effective way to limit the formation of spallations and ultimately of dendrites at relatively large
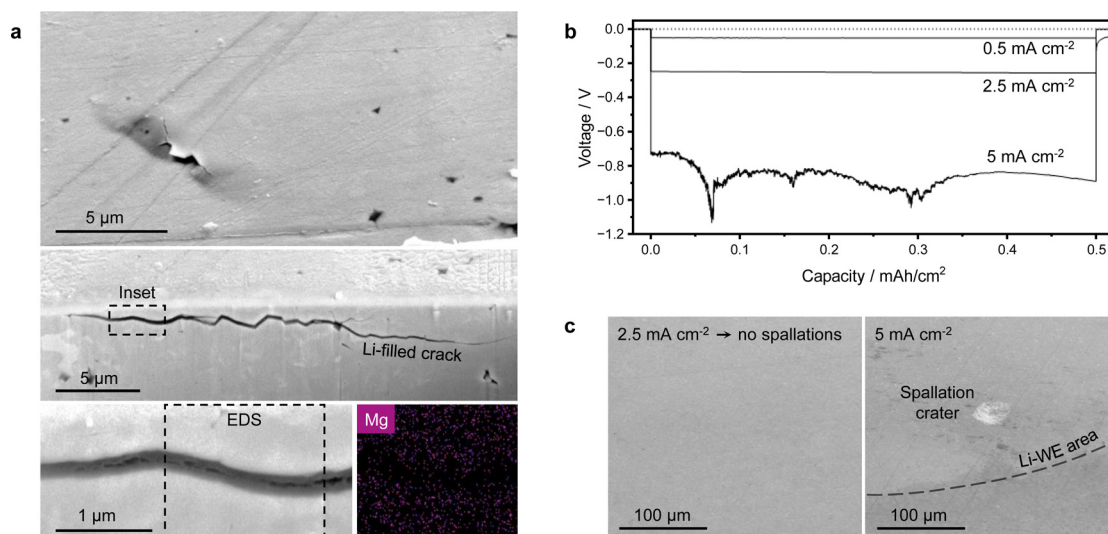

Fig. 4 Current dependency of the spalling process. (a) Top surface and cross-section of a spallation crack after 10 μA h cm^{-2} of plating at a LiMg/LLZTO interface confirming the presence of sub-surface lithium at a very early stage of plating. The serrated crack shape suggests it developed mainly intergranularly. The magnesium EDS signal is absent from the lithium plated in the crack, indicating it was not in contact with the LiMg-WE. (b) Voltage traces at different plating current densities for Li/LLZTO/Li cells with a near-zero starting R_{int}. (c) Secondary electron images of the LLZTO surface after plating 1 mA h cm^{-2} and dissolving the plating electrode in ethanol.

current densities. These results suggest that the same failure mechanism occurs for both lithio-phobic and lithio-philic LLZTO after a certain local current density for the formation of surface spallations is reached. Therefore, according to the proposed formation mechanism for surface spallations, there is a 'critical' current density for the deposition of lithium in occluded pores within the SE. The current dependency of the isolated lithium deposition agrees well with previous modeling work on solid electrolytes.[13]

This study contributes to the understanding of the short-circuiting mechanism of LLZTO and of the relationship between isolated lithium deposition and the nucleation of lithium dendrites. Automated serial sectioning of LLZTO with plasma-FIB in combination with EDS analysis allows to visualize the initiation of dendritic failure with good spatial resolution. We reveal that, above a certain plating current density, spallation cracks form at the interface between LLZTO pellets and the plating electrode. These cracks contain freshly plated lithium that appears to have firstly plated within the SE without physical contact with the electrode. When a LiMg plating electrode is used, magnesium can diffuse into plated lithium that is in physical contact with the electrode. The absence of magnesium in the early-stage spallation cracks demonstrates the physical isolation of these volumes of lithium, indicating that the development of the cracks on the LLZTO surface is directly associated with the deposition of isolated lithium metal in the sub-surface porosity. We propose that the pressure build-up in a sub-surface Li-filled LLZTO pore can be released by opening a circular crack on the SE surface. Then lithium metal preferentially plates in the newly formed crack, which becomes a hot spot for the intensification of both electrical current density and mechanical stress. The insertion of lithium generates further internal pressure and drives crack growth along the mechanically weakest path, eventually creating a continuous short-circuiting path of lithium metal. We used a novel technique, EBIC imaging, to verify that the lithium in the surface spallation cracks can indeed be electrically connected to the short-circuiting lithium dendrite, thus demonstrating that the spallations are directly correlated to the failure of the cell.

The observation that dendrites originate from surface spallations is consistent with a recently proposed two-step mechanism for dendrite initiation and propagation in SEs.[11] Our study shows how the isolated lithium deposits play a role for the initiation of dendrites, emphasizing the significance of limiting this isolated lithium deposition to suppress LLZTO failure. This can be achieved, for instance, by enhancing SE density, which will have the additional benefit of improving the SE mechanical properties, or reducing the local current density at the Li/LLZTO interface by optimizing the LLZTO surface preparation as we have demonstrated. Further investigations are needed to explore whether also the propagation step is affected by lithium deposition in occluded volumes ahead of the dendrite crack, or whether dendritic propagation is a purely mechanical process as recently suggested.[45] Moreover, the precise mechanism of current leakage in SEs remains not fully understood and should be the subject of further studies.

Methods

Sintering of LLZTO

$Li_{6.4}La_3Zr_{1.4}Ta_{0.6}O_{12}$ powder purchased from Ampcera (99.9%, D50 $\sim$5 μm) was cold-pressed in a graphite die and then spark-plasma sintered (Dr Fritsch DSP 507) into dense pellets at 1000, 1100 or 1200 °C and 50 MPa for 5 minutes. Circular pellets were cut into smaller pieces using a low-speed diamond saw, to ensure high sample consistency. The pellets were dry polished in an Ar-filled glovebox (O_2 and H_2O < 0.1 ppm) down to 1 μm with a diamond lapping film until the surface was visually shiny. Pellets of $\sim$1.2 mm thickness were used. To obtain a near-zero starting R_{int}, a rapid acid treatment of 10 seconds in 1 M $HCl_{(aq)}$ was employed immediately prior to cell assembly to remove the surface Li_2CO_3 and LiOH contamination on the LLZTO pellets.[32]

Synthesis of LiMg

Lithium metal (foil, 99.9%, Alfa Aesar) was heated in a stainless-steel crucible to 400 °C in a tube furnace (MTI KSL-1200X-J-UL) within a glovebox. The molten lithium was removed from the furnace once at temperature, any slag carefully removed with a stainless-steel spatula, and an appropriate mass of magnesium metal (turnings, 99.98%, Alfa Aesar) was fully dissolved in the molten lithium. The crucible was then returned to the furnace for 2 hours before slowly cooling to room temperature. Inductively coupled plasma optical emission spectroscopy (ICP-OES) analysis (PerkinElmer Optima 8000) was then used to confirm the Mg content as 10 at%.

X-ray diffraction

XRD measurements were carried using an Empyrean diffractometer with CuK$_{\alpha 1}$ radiation (Malvern Panalytical) to ensure phase purity of the cubic LLZTO.

X-ray photoelectron spectroscopy

The surface of LLZTO was characterised using an ULVAC Phi Versaprobe III XPS with a monochromatic AlK$_\alpha$ source ($h\nu$ 1486.6 eV, 15 kV anode voltage, 25 W beam power, 100 μm beam diameter). The samples were transferred from the glovebox to the XPS in an Ar-filled vessel (ULVAC Phi GmbH). The analysis chamber pressure was maintained below 5×10^{-9} mbar during measurement. The data were energy calibrated relative to the C 1s adventitious carbon signal at 285 eV.

Cell assembly and cycling

Two-electrode cells were assembled with 200 μm thick Li or LiMg electrodes, which were scraped to remove the surface contamination and gently pressed onto the SE after applying 2 mm $\varnothing$ polyimide tape masks to ensure a constant electrode area during cycling. Na/β-Al_2O_3(Ionotec)/Na cells were assembled similarly. The cells with acid-treated LLZTO were heated at 170 °C for 2 hours to further improve the Li/LLZTO contact. All cells were sealed in Mylar pouch bags with Cu current collectors and removed from the glovebox for testing. Galvanostatic cycling and *operando* galvanostatic electrochemical impedance spectroscopy was performed

using a BioLogic SP-200 potentiostat (7 MHz to 500 mHz with a 0.05 mA cm^{-2} perturbation) at 30 °C within a temperature control chamber and with 5 MPa of external stack pressure. Potentiostatic electrochemical impedance spectroscopy was performed with a BioLogic MTZ-35 impedance analyser (3.7 MHz to 1 Hz with a 10 mV perturbation). The impedance spectra were fitted using an equivalent circuit model in the ZView software package.

Conductivity measurements

Ni electrodes 100 nm thick and 2 mm in diameter were RF sputtered using an MBraun MB EVAP built within a glovebox. For the ionic conductivity, EIS at different temperatures was collected on Ni/LLZTO/Ni cells using an MTZ-35 impedance analyser (BioLogic). For the electronic conductivity, a step potential was applied to Ni/LLZTO/Ni cells and the current was measured with a SP-200 potentiostat (BioLogic).

EBIC imaging

A 100 μm ⌀ polyimide tape laser-cut mask was used to define the Li-WE area and limit the number of surface spallation cracks to probe. The cells were cycled until short-circuit, then the Li-WE was carefully peeled off. The Li-CE was electrically connected to the SEM sample holder with Ag paste. A Zeiss NVision 40 FIB-SEM was employed together with an Oxford Instruments Omniprobe100 micromanipulator, connected to a Point Electronic EBIC current amplifier. The sample was exposed to air for a few seconds during loading. EBIC images were acquired at 20 kV accelerating voltage using the software package DISS 5 (Point Electronic).

Plasma-FIB cross-sectioning

Both electrodes were removed after cycling and the LLZTO pellets were transferred to the plasma-FIB (Helios G4 PFIB CXe DualBeam, Thermo Scientific) in an Ar-filled vessel (Gatan iLoad). A Pt-C capping layer was deposited in situ to protect the surface prior to milling with the Xe^{+} beam. A 30 kV, 15 nA focused ion beam was used to mill the cross-section, while a 10 kV, 0.2–0.8 nA electron beam was used for imaging. The SEM and EDS cross-sectional images in the manuscript were collected at an angle of 52°. When a cryo-stage was used, the stage temperature was −150 °C.

Finite element modeling of the electric field

To model the effect of a spallation on the current-density distribution, COMSOL Multiphysics was used to simulate the electric field within a rectangular block of SE of $20 \times 30 \times 50~\mu m^3$, sandwiched between two voltage-biased lithium electrodes. The geometry of the Li/SE interface was restructured from the plasma-FIB sectioning in Fig. 1d using Avizo 3D. The finite element mesh was generated and refined using Blender 3.5 and Instant Meshes.[46] The mesh of the Li/LLZTO interface contained 43311 triangles with a minimum size of 0.1 μm to provide a sufficient resolution of surface morphology. Electric potential in the electrolyte Φ is governed by Laplace's equation $\nabla^2\Phi = 0$. Dirichlet boundary conditions (constant potential) were imposed at the Li/SE interface. No-flux Neumann conditions were imposed at other boundaries $\left(\vec{\nabla}\Phi = 0\right)$. The current density is proportional to the gradient of electric potential according to Ohms law $\vec{i} = \sigma\vec{\nabla}\Phi$.

Author contributions

M. S. conceived and conducted the experimental work. Y. S. and S. R. B. helped with the EBIC imaging. G. L. assisted with the 3D surface reconstruction and conducted the modeling. J. S. G. performed the XPS studies. M. S., C. R. M. G. wrote the manuscript, with contributions and revisions from all authors. The project was supervised by S. S. and C. R. M. G.

Conflicts of interest

The authors declare no competing interests.

Acknowledgements

References

1 T. Krauskopf, F. H. Richter, W. G. Zeier and J. Janek, Physicochemical concepts of the lithium metal anode in solid-state batteries, Chem. Rev., 2020, 120(15), 7745–7794.

2 T. Famprikis, P. Canepa, J. A. Dawson, M. S. Islam and C. Masquelier, Fundamentals of inorganic solid-state electrolytes for batteries, Nat. Mater., 2019, 18(12), 1278–1291.

3 J. Janek and W. G. Zeier, Challenges in speeding up solid-state battery development, Nat. Energy, 2023, 8, 1–11.

4 K. B. Hatzell, X. C. Chen, C. L. Cobb, N. P. Dasgupta, M. B. Dixit, L. E. Marbella, M. T. McDowell, P. P. Mukherjee, A. Verma and V. Viswanathan, et al., Challenges in lithium metal anodes for solid-state batteries, ACS Energy Lett., 2020, 5(3), 922–934.

5 T. Krauskopf, H. Hartmann, W. G. Zeier and J. Janek, Toward a fundamental understanding of the lithium metal anode in solid-state batteries—an electrochemo-mechanical study on the garnet-type solid electrolyte $Li_{6.25}Al_{0.25}La_3Zr_2O_{12}$, ACS Appl. Mater. Interfaces, 2019, 11(15), 14463–14477.

6 H. Wang, H. Gao, X. Chen, J. Zhu, W. Li, Z. Gong, Y. Li, M.-S. Wang and Y. Yang, Linking the defects to the formation and growth of Li dendrite in all-solid-state batteries, Adv. Energy Mater., 2021, 11(42), 2102148.

7 A. Sharafi, H. M. Meyer, J. Nanda, J. Wolfenstine and J. Sakamoto, Characterizing the Li-Li$_7$La$_3$Zr$_2$O$_{12}$ interface stability and kinetics as a function of temperature and current density, *J. Power Sources*, 2016, **302**, 135–139.

8 G. McConohy, X. Xu, T. Cui, E. Barks, S. Wang, E. Kaeli, C. Melamed, X. W. Gu and W. C. Chueh, Mechanical regulation of lithium intrusion probability in garnet solid electrolytes, *Nat. Energy*, 2023, **8**(3), 241–250.

9 L. Barroso-Luque, Q. Tu and G. Ceder, An analysis of solid-state electrodeposition-induced metal plastic flow and predictions of stress states in solid ionic conductor defects, *J. Electrochem. Soc.*, 2020, **167**(2), 020534.

10 L. Porz, T. Swamy, B. W. Sheldon, D. Rettenwander, T. Frömling, H. L. Thaman, S. Berendts, R. Uecker, W. C. Carter and Y.-M. Chiang, Mechanism of lithium metal penetration through inorganic solid electrolytes, *Adv. Energy Mater.*, 2017, 7(20), 1701003.

11 Z. Ning, G. Li, D. L. R. Melvin, Y. Chen, J. Bu, D. Spencer-Jolly, J. Liu, B. Hu, X. Gao and J. Perera, *et al.*, Dendrite initiation and propagation in lithium metal solid-state batteries, *Nature*, 2023, **618**(7964), 287–293.

12 R. Raj and J. Wolfenstine, Current limit diagrams for dendrite formation in solid-state electrolytes for Li-ion batteries, *J. Power Sources*, 2017, **343**, 119–126.

13 Q. Shi, T. Chakravarthy and S. Ceder, G., Understanding metal propagation in solid electrolytes due to mixed ionic-electronic conduction, *Matter*, 2021, **4**(10), 3248–3268.

14 F. Han, A. S. Westover, J. Yue, X. Fan, F. Wang, M. Chi, D. N. Leonard, N. J. Dudney, H. Wang and C. Wang, High electronic conductivity as the origin of lithium dendrite formation within solid electrolytes, *Nat. Energy*, 2019, **4**(3), 187–196.

15 J. Gao, J. Zhu, X. Li, J. Li, X. Guo, H. Li and W. Zhou, Rational design of mixed electronic-ionic conducting Ti-doping Li$_7$La$_3$Zr$_2$O$_{12}$ for lithium dendrites suppression, *Adv. Funct. Mater.*, 2021, **31**(2), 2001918.

16 M. Sun, T. Liu, Y. Yuan, M. Ling, N. Xu, Y. Liu, L. Yan, H. Li, C. Liu and Y. Lu, *et al.*, Visualizing lithium dendrite formation within solid-state electrolytes, *ACS Energy Lett.*, 2021, **6**(2), 451–458.

17 H. Buschmann, J. Dölle, S. Berendts, A. Kuhn, P. Bottke, M. Wilkening, P. Heitjans, A. Senyshyn, H. Ehrenberg and A. Lotnyk, *et al.*, Structure and dynamics of the fast lithium ion conductor 'Li$_7$La$_3$Zr$_2$O$_{12}$', *Phys. Chem. Chem. Phys.*, 2011, **13**(43), 19378–19392.

18 B. Shao, Y. Huang and F. Han, Electronic conductivity of lithium solid electrolytes, *Adv. Energy Mater.*, 2023, **13**(16), 2204098.

19 M. Philipp, B. Gadermaier, P. Posch, I. Hanzu, S. Ganschow, M. Meven, D. Rettenwander, G. J. Redhammer and H. M. R. Wilkening, The electronic conductivity of single crystalline Ga-stabilized cubic Li$_7$La$_3$Zr$_2$O$_{12}$, a technologically relevant parameter for all-solid-state batteries, *Adv. Mater. Interfaces*, 2020, **7**(16), 2000450.

20 H.-K. Tian, Z. Liu, Y. Ji, L.-Q. Chen and Y. Qi, Interfacial electronic properties dictate Li dendrite growth in solid electrolytes, *Chem. Mater.*, 2019, **31**(18), 7351–7359.

21 T. Thompson, S. Yu, L. Williams, R. D. Schmidt, R. Garcia-Mendez, J. Wolfenstine, J. L. Allen, E. Kioupakis, D. J. Siegel and J. Sakamoto, Electrochemical window of the Li-ion solid electrolyte Li$_7$La$_3$Zr$_2$O$_{12}$, *ACS Energy Lett.*, 2017, **2**(2), 462–468.

22 C. Zhu, T. Fuchs, S. A. Weber, F. H. Richter, G. Glasser, F. Weber, H.-J. Butt, J. Janek and R. Berger, Understanding the evolution of lithium dendrites at Li$_{6.25}$Al$_{0.25}$La$_3$Zr$_2$O$_{12}$ grain boundaries via *operando* microscopy techniques, *Nat. Commun.*, 2023, **14**(1), 1300.

23 X. Liu, R. Garcia-Mendez, A. R. Lupini, Y. Cheng, Z. D. Hood, F. Han, A. Sharafi, J. C. Idrobo, N. J. Dudney and C. Wang, *et al.*, Local electronic structure variation resulting in Li 'filament' formation within solid electrolytes, *Nat. Mater.*, 2021, **20**(11), 1485–1490.

24 H.-K. Tian, B. Xu and Y. Qi, Computational study of lithium nucleation tendency in Li$_7$La$_3$Zr$_2$O$_{12}$ (LLZO) and rational design of interlayer materials to prevent lithium dendrites, *J. Power Sources*, 2018, **392**, 79–86.

25 H. Kim, P. Conlin, M. Bergschneider, H. Chung, S. Y. Kim, S. W. Cha, M. Cho and K. Cho, First principles study on li metallic phase nucleation at grain boundaries in a lithium lanthanum titanium oxide (llto) solid electrolyte, *J. Mater. Chem. A*, 2023, **11**(6), 2889–2898.

26 F. Shen, M. B. Dixit, X. Xiao and K. B. Hatzell, Effect of pore connectivity on Li dendrite propagation within LLZO electrolytes observed with synchrotron X-ray tomography, *ACS Energy Lett.*, 2018, **3**(4), 1056–1061.

27 J. Tippens, J. C. Miers, A. Afshar, J. A. Lewis, F. J. Q. Cortes, H. Qiao, T. S. Marchese, C. V. Di Leo, C. Saldana and M. T. McDowell, Visualizing chemomechanical degradation of a solid-state battery electrolyte, *ACS Energy Lett.*, 2019, **4**(6), 1475–1483.

28 S. Hao, J. J. Bailey, F. Iacoviello, J. Bu, P. S. Grant, D. J. Brett and P. R. Shearing, 3D imaging of lithium protrusions in solid-state lithium batteries using X-ray computed tomography, *Adv. Funct. Mater.*, 2021, **31**(10), 2007564.

29 C. Wang, K. Fu, S. P. Kammampata, D. W. McOwen, A. J. Samson, L. Zhang, G. T. Hitz, A. M. Nolan, E. D. Wachsman and Y. Mo, *et al.*, Garnet-type solid-state electrolytes, materials, interfaces, and batteries, *Chem. Rev.*, 2020, **120**(10), 4257–4300.

30 T. Krauskopf, R. Dippel, H. Hartmann, K. Peppler, B. Mogwitz, F. H. Richter, W. G. Zeier and J. Janek, Lithium-metal growth kinetics on LLZO garnet-type solid electrolytes, *Joule*, 2019, **3**(8), 2030–2049.

31 A. Sharafi, E. Kazyak, A. L. Davis, S. Yu, T. Thompson, D. J. Siegel, N. P. Dasgupta and J. Sakamoto, Surface chemistry mechanism of ultra-low interfacial resistance in the solid-state electrolyte Li$_7$La$_3$Zr$_2$O$_{12}$, *Chem. Mater.*, 2017, **29**(18), 7961–7968.

32 H. Huo, Y. Chen, N. Zhao, X. Lin, J. Luo, X. Yang, Y. Liu, X. Guo and X. Sun, In-situ formed Li$_2$CO$_3$-free garnet/Li interface by rapid acid treatment for dendrite-free solid-state batteries, *Nano Energy*, 2019, **61**, 119–125.

33 J. Kasemchainan, S. Zekoll, D. Spencer Jolly, Z. Ning, G. O. Hartley, J. Marrow and P. G. Bruce, Critical stripping

This journal is © The Royal Society of Chemistry 2024

Energy Environ. Sci., 2024, **17**, 2431–2440 | **2439**

current leads to dendrite formation on plating in lithium anode solid electrolyte cells, *Nat. Mater.*, 2019, **18**(10), 1105–1111.

34 Z. Ning, D. S. Jolly, G. Li, R. De Meyere, S. D. Pu, Y. Chen, J. Kasemchainan, J. Ihli, C. Gong and B. Liu, *et al.*, Visualizing plating-induced cracking in lithium-anode solid–electrolyte cells, *Nat. Mater.*, 2021, **20**(8), 1121–1129.

35 E. Kazyak, R. Garcia-Mendez, W. S. LePage, A. Sharafi, A. L. Davis, A. J. Sanchez, K.-H. Chen, C. Haslam, J. Sakamoto and N. P. Dasgupta, Li penetration in ceramic solid electrolytes, *operando* microscopy analysis of morphology, propagation, and reversibility, *Matter*, 2020, **2**(4), 1025–1048.

36 R. Choudhury, M. Wang and J. Sakamoto, The effects of electric field distribution on the interface stability in solid electrolytes, *J. Electrochem. Soc.*, 2020, **167**(14), 140501.

37 J. Zhao, Y. Tang, Q. Dai, C. Du, Y. Zhang, D. Xue, T. Chen, J. Chen, B. Wang and J. Yao, *et al.*, In situ observation of Li deposition-induced cracking in garnet solid electrolytes, *Energy Environ. Mater.*, 2022, **5**(2), 524–532.

38 M. Nagao, A. Hayashi, M. Tatsumisago, T. Kanetsuku, T. Tsuda and S. Kuwabata, In situ SEM study of a lithium deposition and dissolution mechanism in a bulk-type solid-state cell with a Li2S-P2S5 solid electrolyte, *Phys. Chem. Chem. Phys.*, 2013, **15**(42), 18600–18606.

39 R. Zhou, M. Yu, D. Tweddle, P. Hamer, D. Chen, B. Hallam, A. Ciesla, P. P. Altermatt, P. R. Wilshaw and R. S. Bonilla, Understanding and optimizing EBIC pn-junction characterization from modeling insights, *J. Appl. Phys.*, 2020, **127**(2), 024502.

40 M. Siniscalchi, J. Liu, J. S. Gibson, S. J. Turrell, J. Aspinall, R. S. Weatherup, M. Pasta, S. C. Speller and C. R. M. Grovenor, On the relative importance of Li bulk diffusivity and interface morphology in determining the stripped capacity of metallic anodes in solid-state batteries, *ACS Energy Lett.*, 2022, **7**(10), 3593–3599.

41 T. Krauskopf, B. Mogwitz, C. Rosenbach, W. G. Zeier and J. Janek, Diffusion limitation of lithium metal and Li-Mg alloy anodes on LLZO type solid electrolytes as a function of temperature and pressure, *Adv. Energy Mater.*, 2019, **9**(44), 1902568.

42 T. Tang and M. Chaudhri, Electrical degradation of β-alumina, *J. Mater. Sci.*, 1982, **17**, 157–163.

43 L. De Jonghe, L. Feldman and A. Beuchele, Slow degradation and electron conduction in sodium/beta-aluminas, *J. Mater. Sci.*, 1981, **16**, 780–786.

44 J. Z. Lee, T. A. Wynn, M. A. Schroeder, J. Alvarado, X. Wang, K. Xu and Y. S. Meng, Cryogenic focused ion beam characterization of lithium metal anodes, *ACS Energy Lett.*, 2019, **4**(2), 489–493.

45 C. D. Fincher, C. E. Athanasiou, C. Gilgenbach, M. Wang, B. W. Sheldon, W. C. Carter and Y.-M. Chiang, Controlling dendrite propagation in solid-state batteries with engineered stress, *Joule*, 2022, **6**(12), 2794–2809.

46 W. Jakob, M. Tarini, D. Panozzo and O. Sorkine-Hornung, *et al.*, Instant field-aligned meshes, *ACM Trans. Graph.*, 2015, **34**(6), 189.

2440 | *Energy Environ. Sci.*, 2024, **17**, 2431–2440

This journal is © The Royal Society of Chemistry 2024